Seismic anisotropy reveals stress changes around a fault as it is activated by hydraulic fracturing

Nadine Igonin[1,3*], James P. Verdon[2], David W. Eaton[3]

1. Jackson School of Geoscience, University of Texas at Austin, Austin, Texas, USA.

2. School of Earth Sciences, University of Bristol, Wills Memorial Building, Queen's Road, Bristol, UK.

3. Department of Geoscience, University of Calgary, Calgary, Alberta, Canada.

* Corresponding Author. Email: nadine.igonin@austin.utexas.edu

Manuscript in preparation for Seismological Research Letters

Earlier version published/presented at IMAGE 2021

Declaration of Competing Interests:

The authors acknowledge there are no conflicts of interest recorded.

ABSTRACT

Subsurface stress conditions evolve in response to earthquakes or fluid injection/withdrawal. Using observations of an induced seismicity sequence from a dense local array, anisotropy analysis is employed to characterise stress changes around a fault. The dataset comprises high signal to noise ratio S-wave data from 300 events, ranging in magnitude from -0.45 to 4.1, recorded on 98 3-C geophones cemented in shallow wells. It is found that the orientation of the fast S-wave direction remains relatively constant for all the stations over time, but the magnitude of the anisotropy, as measured by the delay time between the fast and slow S-wave, exhibits significant local variations. Some stations experience a systematic increase or decrease in the delay time, with a spatial coherence about the injection well. The stress changes due to hydraulic fracturing, aseismic slip and the observed earthquakes are modelled to determine the best fit to the observed anisotropy changes. Our analysis indicates that the creation of a network of tensile hydraulic fractures during fluid injection is likely to be the cause of the observed anisotropy changes. This study confirms that measurements of seismic anisotropy over time reflects the evolving stress state of a fault prior to and during rupture.

1. INTRODUCTION

Induced seismicity caused by subsurface fluid injection has been generated by a range of industries, including hydraulic fracturing for shale gas (e.g., Bao and Eaton, 2016; Clarke et al., 2019; Verdon and Bommer, 2021), oilfield waste-water disposal (e.g., Ellsworth, 2013), CO_2 sequestration (e.g., Stork et al., 2015), geothermal energy (e.g., Buijze et al., 2019), and natural gas storage (e.g., Ruiz-Barajas et al., 2017). There is a clear and pressing need to better understand the perturbations caused by subsurface injection activities, and how these perturbations result in the activation of faults and the occurrence of induced seismicity (Atkinson et al., 2020, Schultz et al., 2020).

Hydraulic fracturing perturbs the state of stress in the subsurface in a number of ways. The elevated pore pressures associated with fluid injection reduces the effective normal stresses, while leaving shear stress essentially unchanged. In low-permeability shale formations, the volume influenced by pore pressure increases is generally limited to a region in close proximity to the injection well, unless pre-existing high permeability fracture corridors are present to act as a hydraulic conduit (e.g., Riazi and Eaton, 2020; Igonin et al., 2021). By design, the process of hydraulic fracturing creates fractures that open in a tensile manner (mode 1 failure). This tensile opening perturbs the stress field in the surrounding rocks (e.g., Kettlety et al., 2020).

The direct stress changes created by the hydraulic fracturing may cause slip on pre-existing structural features such as natural fractures and faults. This slip may be accommodated as aseismic slip, low-magnitude microseismicity, or as larger-magnitude induced seismicity (Eaton, 2018). Slip on pre-existing fractures or faults (whether seismic or aseismic) can create further stress perturbations in the subsurface (e.g., Kettlety et al., 2019) that, in turn, causes additional fault reactivation in a cascading effect (e.g., Eyre et al., 2019a; 2020; Peña Castro et al., 2020).

To date, imaging the relative contributions of these different perturbations has proved challenging. Typically, the locations of observed events are compared with modelled stress perturbations to investigate whether the observed events fall within regions that have experienced positive Coulomb Failure Stress (ΔCFS),

$$\Delta CFS = \Delta\tau - \mu_f(\Delta\sigma_n - \Delta P), \quad (1)$$

where $\Delta\tau$ is the change in shear stress, $\Delta\sigma_n$ is the change in normal stress, ΔP is the change in pore pressure, and μ_f is the coefficient of friction (e.g., Stein, 1999; Steacy et al., 2004).

However, for hydraulic fracturing cases, the results may be non-unique, making it difficult to fully constrain geomechanical processes associated with fault reactivation and induced seismicity (e.g., Deng et al., 2016; Schultz et al., 2017). Discriminating between different potential fault reactivation mechanisms is of paramount importance, since they have differing implications for mitigation. For example, if faults are being reactivated by direct pressurisation of pore fluids, then an improved understanding of subsurface hydrology is required (e.g., Igonin et al., 2021), whereas if poroelastic stress transfer is the key process causing fault reactivation, then a better understanding of subsurface geomechanics, and the relative positions and orientations of wells, hydraulic fractures, and faults may be required (e.g., Kettlety et al., 2020).

In order to assess the impact of hydraulic fracturing and fault activation on the subsurface stress state, we explore the possibility of using changes in seismic anisotropy. To do so, we use shear wave splitting (SWS) measurements from microseismic waveforms recorded during stimulation (Verdon et al., 2009). Seismic anisotropy is generated by the alignment of fabrics such as sedimentary layering (e.g., Baird et al., 2017), fracture networks (e.g., Verdon et al., 2009), and stress-induced microcracks (e.g., Verdon et al., 2008) in the subsurface. In the immediate vicinity of rocks where new hydraulic fractures are being created, changes in anisotropy will be driven by the generation of new fracture networks, and SWS observations have been used to image and characterise hydraulic fractures (e.g., Verdon et al., 2010; Wuestefeld et al., 2011; Verdon and Wuestefeld, 2013; Baird et al., 2013; Gajek et al., 2018). Away from the immediate vicinity of the hydraulic fractures, however, we do not expect to see any significant alterations to structural fabrics, and so any changes in seismic anisotropy must be driven by changes in the *in situ* stress field. Such stress changes will act to preferentially open or close microcracks and fractures, leading to changes in the strength and polarization of seismic anisotropy (e.g., Crampin, 1987; Zatsepin and Crampin, 1997; Verdon et al., 2008).

In this study we analyse the Waskahigan microseismic dataset, which was recorded by a dense surface array deployed to monitor hydraulic fracturing of the Duvernay Shale Formation in the Fox Creek area, Alberta, Canada. In this area, hydraulic fracturing in the Duvernay Shale formation has generated induced seismicity (e.g., Bao and Eaton, 2016; Igonin et al., 2021), and the regulator has imposed a Traffic Light Protocol for induced seismicity mitigation (AER, 2015). At the site studied here, the largest event reached magnitude M_W 4.1, exceeding the red-light threshold and resulting in the cessation of operations (Eyre et al., 2019b). Temporal changes in SWS have already been observed at the site (Li et al., 2019) using data from four broadband seismograph stations.

We perform SWS measurements on microseismic events observed using a dense surface array of over 90 stations. We find evidence for precursory and co-seismic changes in SWS associated with a M_W 4.1 induced event. Some regions experienced an increase in anisotropy strength, while other areas experienced a decrease. To interpret our SWS observations, we produce models of the stress perturbations that would be created by different geomechanical processes, including tensile hydraulic fracture opening, microseismic slip on pre-existing faults, and aseismic slip on faults. The relative ability of these different mechanisms to account for the observed anisotropy changes provides important inferences with respect to their relative importance in reactivating the fault that produced the M_W 4.1 mainshock.

2. DATASET

The Waskahigan dataset used in this study is from near Fox Creek, Alberta, where hydraulic fracturing has been conducted in the Devonian-age Duvernay Formation. This site was one of the first in the area to experience an earthquake above magnitude 4.0 (Bao and Eaton, 2016). This dataset has been the focus of several publications (e.g. Wang et al., 2016; Li et al., 2019; Eyre et al., 2019a;b; 2020). A dense surface microseismic monitoring array was deployed, providing high quality microseismic observations that have been used to image fault reactivation by hydraulic fracturing. The largest event (M_W 4.1), occurred on January 12, 2016, during stimulation of the 26th injection stage. This event occurred towards to the heel of the well, as shown in Figure 1. As a result of this event, which exceeded the red-light threshold (Kao et al., 2018), further operations were suspended at this site.

Figure 1a shows the geometry of the seismic monitoring stations in relation to the single well that was completed. At each of the 98 stations, a 4.5 Hz 3-component geophone was cemented at the bottom of a 27 m deep borehole. The average station separation is less than 500 m; this dense station coverage is advantageous for detailed spatial mapping of anisotropy. A study of anisotropy at this site has been performed at this site by Li et al. (2019), using data from four broadband seismometer stations (WSK01-04), which are labelled in Figure 1a. The Li et al. (2019) results are further examined in our discussion section.

The shallow borehole array was active for 17 days, from December 29, 2015 to January 16, 2016. A catalog processed by a commercial contractor identified 9,769 microseismic events that occurred during that period (Figure 1). A limited amount of operational microseismicity (i.e., generally weak, $M < 0$ event clouds that align with hydraulic fractures) was observed. The bulk of the observed seismicity was associated with the activation of a complex fault structure to the east of the well. Several fault strands can be identified by examining lineations revealed by the microseismic event locations. In particular, a trend of events beginning near to the toe of the well, and extending approximately 1.7 km in a NNE direction, represents the first structure to activate. A second fault structure, with a N-S strike, can be seen towards the heel of the well, on which the M_W 4.1 mainshock occurred. The focal mechanisms for the three largest events (M_W 2.2, M_W 2.6 and M_W 4.1) can be seen in Figure 1b, and they are right-lateral strike-slip mechanisms for which the primary nodal plane aligns with the first and second fault structures. A number of smaller structures can also be identified. Much of the reactivated fault structures, as imaged by the microseismicity, occurred in the Ireton and Wabamun Formations which overly the Duvernay. The faults imaged by the microseismicity are consistent with faults imaged by reflection seismic surveys at the site (Eyre et al., 2019a). The regional stress field in this area is characterised by S_{Hmax} orientation that is approximately NE-SW (045°), but some local variability in this orientation has been observed (e.g., Igonin et al., 2021).

Eyre et al. (2019a) studied the microseismicity at this site and noted that the bulk of the seismicity was observed in the strata overlying the Duvernay Formation, with gaps in the microseismicity between where stimulation was taking place, and where the resulting seismicity was observed. The faults on which the seismicity occurred were observed in the 3D reflection seismic data to extend through the Duvernay into the overlying strata. They inferred that the depth gap in microseismicity was generated by aseismic slip of the fault strands within the Duvernay Formation, with this aseismic slip then promoting seismic ruptures in the overlying Ireton and Wabamun Formations. Eyre et al. (2019a) argued that this aseismic slip outpaced the impacts of direct pore pressure communication along the faults. However, they did not examine any of the other potential mechanisms for generating fault slip that we describe above, and they did not present any independent observations to show whether or not this aseismic slip did take place.

3. SWS ANALYSIS

When a shear wave passes through an anisotropic material, it is split into orthogonally-polarised waves that travel with different velocities. This shear wave splitting is typically characterised by measurements of the delay time between the fast and slow waves, δt, and the orientation of the fast S-wave polarisation, ψ. The delay time is typically normalised by the S-wave path length, D, and the average S-wave velocity along the path, V_{Savg}, to give the percentage difference between fast and slow S-wave velocities, δV_S:

$$\delta V_S = 100 \times \frac{\delta t \times V_{Savg}}{D}. \quad (2)$$

In this study we assume a straight-line path from event to receiver when performing the normalisation, rather than computing ray-bending effects. The average S-wave velocity is calculated for each event, and ranges between 1927 – 1965 m/s.

We performed SWS measurements on the recorded horizontal components of particle velocity, using 300 of the largest events, where signal-to-noise ratios were highest. The smallest event used in the analysis had a magnitude of −0.45. We used the semi-automated multi-windowing method described Teanby et al. (2004) to perform the measurements and to quality control the results. Further details are provided in the Supplementary Materials. This procedure produced 5,931 good quality SWS measurements from the 28,800 individual event-receiver combinations (300 events × 96 receivers).

Figure 2 shows orientation of ψ for all of the SWS measurements at each station. We find that the results for ψ are very consistent at each station, while there is variability between stations, with ψ generally striking NNE-SSW, but varying from N-S to ENE-WSW. We did not observe any significant temporal variations in ψ. The spatial variations in ψ may reflect either local variations in natural fracture orientations, or variations in S_{Hmax} orientation in response to nearby reefs (just south of the study area) and the faults on which seismicity was observed (Eyre et al., 2019b).

In contrast to the ψ measurements, many stations showed clear temporal variations in the path-averaged S-wave anisotropy strength, δV_S. Examples from four stations are shown in Figure 3. Some stations showed changes in δV_S prior to the M_W 4.1 mainshock, and others showed coseismic changes with the mainshock. Some stations showed δV_S changes both prior to the mainshock and during it. The temporal variations for all of the stations are shown in the Supplementary Material and discussed further therein. In Figure 4 we plot the overall trends observed for every station. We note clear and coherent spatial distributions of stations that experienced either increases or decreases in δV_S. Both prior to the M_W 4.1 mainshock and during it, stations that experienced an increase is δV_S are found to the north and west of the stimulated region, while stations that experienced a decrease in δV_S are found to the south and east of the stimulated region. More stations experienced δV_S changes prior to the M_W 4.1 mainshock than coseismically with it, and in general the δV_S changes prior to the M_W 4.1 event were of larger magnitude than those that occurred coseismically.

Previous observations of temporal SWS changes during hydraulic fracturing have been interpreted with respect to changing structural fabrics created by hydraulic fracture propagation (e.g., Verdon et al., 2010; Verdon and Wuestefeld, 2013; Baird et al., 2013). However, those examples have used downhole receivers placed in the reservoir, such that most of the raypaths were through rocks directly affected by the hydraulic stimulation.

In contrast, for this study events were monitored with a surface array, so most of the raypath is through the overburden. Moreover, most of the events used in our SWS analysis occurred above the injection zone (the Duvernay Formation) in the Ireton and Wabamum Formations. As such, we do not anticipate the volume of rock through which the seismic waves have passed to have experienced significant changes in structural fabric (i.e., the formation of pervasive new sets of fractures). Since we do not anticipate significant generation of new structural fabrics in the rock volume traversed by the seismic waves, any temporal changes in anisotropy must, by a process of elimination, be caused by modulations of fracture or microcrack densities within the overburden resulting from stress changes produced by deformation within the reservoir and within the overlying fault system. In the following section we develop deformation models for a selection of different geomechanical processes that may have acted within the reservoir during the hydraulic stimulation in order to assess the extent to which they may have contributed to the observed SWS changes.

4. Stress Perturbation Models

We consider five potential sources of stress perturbation that could have created the changes in seismic anisotropy in the layers overlying the reservoir: tensile hydraulic fracture opening; microseismicity; aseismic fault slip; dilatant fault opening; and coseismic slip associated with the M_W 4.1 mainshock event (Table 1). We use the PSCMP code developed by Wang et al. (2006), which uses the Okada (1992) equations to model stress perturbations. We compute stress changes throughout the rock volume around the well. In all of the following models, we use Lamé parameters of λ = 25 GPa and G = 25 GPa, and a friction coefficient of μ_f = 0.7, and a Skempton coefficient of 0.4. In the Supplementary Materials, we perform a sensitivity analysis to these parameters, finding that the choice of values has little impact on the resulting modelled anisotropy changes.

4.1 Tensile hydraulic fracture opening

The tensile opening of hydraulic fractures within the reservoir will generate stress changes in the surrounding rock. In this study we follow the method described by Kettlety et al. (2020) whereby, rather than relying on a single model case for the hydraulic fractures, we stochastically sample the parameters that define hydraulic fracture geometries from appropriate statistical distributions (as described in the following paragraph), producing 100 such models and computing the median stress changes at each subsurface point. By doing so, we are able to examine the generic impact of tensile hydraulic fracture opening on the surrounding stress field.

In this case we consider two alternative parameterisations. In the first model, which we refer to the homogenous HF case (HHF), the hydraulic fracturing from each stage follows identical parameterisation, which is based primarily on microseismic observations of hydraulic fracture geometries from other sites within the region. The initiation point for each fracture is positioned relative to the injection point with a normal distribution with a standard deviation of 30 m. Fractures strike in the direction of maximum horizontal stress, either to the NE (45°) or SW (235°), with a standard deviation of 5° from these orientations. All of the fractures are vertical. Fracture lengths are selected from a uniform distribution between 0 – 300 m in length, and have an aspect ratio (i.e. fracture height vs. fracture length) of 0.5. Each fracture accommodates 2 mm of purely tensile opening. The number of fractures is controlled by the injection volume for each stage – we continue to populate fractures according to the aforementioned parameterisation until the total volume of the open fractures matches that of the stage injection volume. Figure 5a shows an example hydraulic fracture model generated by this parameterisation.

From Figure 1, we note that the majority of the observed microseismicity is found to the east of the well. Such asymmetric fracture growth is not uncommon, and may be driven by gradients in the *in situ* stress conditions or geomechanical properties (e.g., Maxwell and Norton, 2012). We also note that the early stages at the toe of the well would have immediately intersected the large, NNE-trending structure. We might expect the intersection with this structure to have limited the length of the resulting hydraulic fractures, and potentially have allowed significant volumes of fluid leak-off to take place. We therefore adjusted our HHF model to take these factors into consideration. In the leak-off hydraulic fracturing model (LOHF), the asymmetry in hydraulic fracture propagation direction is recognised by assigning a 75 % probability that a given HF will propagate to the NE (and a 25 % probability of striking to the SW). All fractures that strike to the SW have a maximum length of 100 m. For the first seven stages, fractures that strike to the NE have a maximum length of L_{MAX} = [50, 55, 60, 65, 100, 100, 100], respectively. All subsequent stages have L_{MAX} = 300 m. For the first ten stages, the effective fluid injection volumes, which we use to define the total number of hydraulic fractures as described above, is reduced by the following leak-off fractions F_{LO} = [0.1, 0.1, 0.1, 0.1, 0.1, 0.5, 0.5, 0.5, 0.5, 0.5]. Figure 5b shows an example hydraulic fracture model generated by this parameterisation, and we note that the resulting modelled hydraulic fractures are constrained such that they do not cross the large NNE-trending structure imaged by the microseismicity.

4.2 Microseismicity

The observed microseismicity, which in this case primarily represents shear slip on pre-existing faults and fractures, will create stress changes in the surrounding rocks. The microseismic contractor who processed these events computed source mechanisms for every identified event. For this study we only utilise events with magnitudes greater than -1.0, since these are more likely to have robust focal mechanisms. Since deformation will scale with magnitude, they represent the largest potential sources of deformation. We examine the coseismic effects of the M_W 4.1 mainshock separately (see below), so for the microseismicity we only consider events prior to the mainshock. Each event is treated as a square slip patch centred on the event hypocentre. The strike, dip and rake for each event are determined from the source mechanisms. We do not have any independent measurement of the rupture area or slip amount. We therefore assume that each event has a stress drop of $\Delta\sigma$ = 1 MPa (we show the impact of using different $\Delta\sigma$ values in the Supplementary Materials), with the rupture area, A, then being determined by the seismic moment, M_O (Kanamori and Brodsky, 2004)

$$A = \left(\frac{M_O}{\Delta\sigma}\right)^{\frac{2}{3}}, \tag{3}$$

and slip d, given by:

$$d = \frac{M_O}{GA}. \tag{4}$$

4.3 Aseismic Slip

As described above, the lack of seismicity within the Duvernay Formation itself, in comparison to the numbers of events located in the overlying Ireton and Wabamun Formations, led Eyre et al. (2019a) to interpret that the mainshock was triggered by a process of aseismic slip. We therefore generate stress transfer models to evaluate this hypothesis. Based on the microseismic observations, we simulate aseismic slip on two structures – the large, c. 1.7 km long NNE-trending structure that reactivated near to the toe of the well, and the N-S trending fault towards the heel of the well on which the mainshock is located. We define 5 aseismic slip patches along the NNE-trending structure (numbered 1 – 5 in Figure 5c), and a single slip patch along the N-S trending fault (numbered 6 in Figure 5c). Following the aseismic slip model presented by Eyre et al. (2019a), we assume that each aseismic slip patch extends from 2,700 to 2,300 mbsl (metres below sea level) depth, and that 2 cm of right-lateral slip occurs on each patch during stimulation.

In addition to aseismic strike-slip motion on these faults, the increased pore pressure within the reservoir could have created dilatant motion. We therefore generated an additional model to simulate this process. The same slip patches as shown in Figure 5c were used. Since the models developed by Eyre et al. (2019a) showed that pore pressures would not extend as far along the faults as the aseismic slip, we modelled the dilatant slip as extending from 2,600 to 2,400 mbsl, with 2 cm of tensile opening taking place.

4.4 M_W 4.1 Mainshock

Since some stations showed a change in anisotropy that is coseismic with the M_W 4.1 mainshock, we also compute the stress perturbations that would be created by this event. We follow the same procedure as described above for the microseismic events to compute the position, dimensions and slip amount for this event (Equations 3 and 4). For the source mechanism of this event, we use the inversion results of Wang et al. (2016), who estimated a strike/dip/rake of 184/82/166°.

4.5 Stress Changes and Anisotropy

For all of the models described above, we use the PSCMP code (Wang et al., 2006) to compute the stress perturbations in the reservoir and surrounding rocks. To make comparisons between the models and the observed anisotropy, we need to consider the impact of stress changes on seismic velocities. In general, increases in compressive stress will produce increases in seismic velocity, as both fractures and grain-boundary microcracks are forced closed (e.g., Verdon et al., 2008). Increases in compressive stress will reduce seismic anisotropy, since it is the alignment of these fractures and microcracks that creates anisotropy in sedimentary rocks. In the following results, we map changes in the mean of the principal stresses, Δp,

$$\Delta p = \frac{\Delta\sigma_1 + \Delta\sigma_2 + \Delta\sigma_3}{3}, \tag{5}$$

where $\Delta\sigma_{1,2,3}$ are the principal components of the change in stress generated by the PSCMP code, where positive Δp denotes a reduction in compressive stress, and a negative Δp denotes an increase in compressive stress. We consider the mean principal stress change because an increase in compressive stress will serve to close cracks and fractures regardless of their orientation, thereby reducing the anisotropy, whereas a decrease in compressive stresses will allow cracks and fractures to open, thereby increasing anisotropy.

The net change in anisotropy measured at a given station will be determined by overall changes along the raypaths travelled to each station. We consider straight line paths from putative event locations within microseismic event to each receiver. For the raypath to each station, we compute the mean value of Δp along this path. We can then compare the modelled changes in stress along given raypaths with the observed changes in anisotropy.

4.6 Results

In Figure 6 we plot maps and cross-sections of the stress changes produced by each of the models described above. The maps are plotted at a depth of 2,100 mbsl, as this represents a depth through which most of the observed raypaths travelled, while the cross-sections are plotted through the centre of the microseismic cloud. We find that the aseismic slip patch and microseismic event models produce similar results, with lobes of increased compressive stress to the northwest and southeast of the stimulated zone, and lobes of reduced compressive stress to the SW and NE of the stimulated zone. The stress changes from the aseismic slip model are generally larger than those produced by the microseismic events. The dilatant fault slip model produces a zone of reduced compressive stresses above the fault, with smaller zones of increased compressive stress to the east and west.

The results from the two tensile hydraulic fracture opening models are similar to each other, and very different to the aseismic slip, microseismicity, and dilatant fault slip results. The hydraulic fracture models have reduced compressive stresses in the region overlying the hydraulic fractures, and increased compressive stresses in the regions to the NW and SE. The coseismic slip model produces lobes of increased compressive stress to the NW and SE of the mainshock location, and decreased compressive stress to the NE and SW. The coseismic stress changes are large, but more spatially limited in extent that the changes produced by the other models.

Figure 7 shows the resulting modelled stress changes along the raypaths to each receiver. For the hydraulic fracturing, aseismic slip, dilatant fault slip, and microseismic models, we compute stress changes along raypaths originating at x = 3,925 m, y = 3,635 m, z = 2,300 mbsl, in the centre of the cloud of microseismic events that occurred before the mainshock. After the mainshock, the loci of microseismicity shifted onto the northernmost fault strand, so for the coseismic model we plot the stress changes along raypaths originating at x = 3,925 m, y = 5,135 m, z = 2,100 mbsl.

The model results presented in Figure 7 allow us to make direct comparisons with the observed δV_S changes at each station. Prior to the occurrence of the M_W 4.1 mainshock, we observed increases in δV_S for stations to the north and west of the well, and decreases in δV_S for stations to the south and east of the well.

The aseismic slip patch model produces relatively small Δp changes in the rocks above the reservoir, and the mean changes in Δp are negative along the raypaths to all stations. Conversely, the dilatant fault slip model and the homogenous hydraulic fracturing model both produce mean changes in Δp that are positive along the raypaths to all stations. Given that the observed anisotropy is observed to increase along some raypaths, and to decrease along others, these models struggle to account for the observed trends in increasing and decreasing δV_S.

The microseismic event model produces a more complicated pattern of negative and positive mean Δp changes, with negative values for receivers close to the well and to the north, and positive values for stations to the south and east. Again, however, this model does not match the trends in δV_S that we observed.

The LOHF model, which accounts for potential fault intersections and leak-off in the growth of hydraulic fractures, produces a pattern of mean Δp changes that has positive values for stations to the north and west of the well, and negative values for stations to the south and east. This broadly matches the pattern of δV_S changes that we observed. It is therefore reasonable to surmise that the changes in anisotropy that we have observed prior to the occurrence of the M_W 4.1 mainshock are consistent with the stress changes that would be produced in the overburden by tensile opening of hydraulic fractures in the reservoir, so long as the hydraulic fractures at the toe of the well are limited by their interaction with the fault which has been mapped by both microseismic and 3D reflection seismic observations.

Figure 7e compares the modelled Δp changes along raypaths to every station with the observed changes in δV_S coseismic with the mainshock. The model produces positive changes in Δp for stations to the NE and SW of the well, and negative changes in Δp for stations to the NW and SE of the well. This does not match the observed coseismic δV_S changes, which have a similar pattern to the δV_S changes observed prior to the mainshock, with increases in δV_S to the NW of the well. In fact, the hydraulic fracturing models, and in particular the LOHF model, produces modelled Δp changes that provide the closest match to the δV_S observations. We therefore suggest that the coseismic δV_S observations do not represent a substantial change in deformation produced by the M_W 4.1 event, but simply represent a continuation of the deformation produced by the propagation of hydraulic fractures.

In the following section, we explore the implications of the observed anisotropy trends and how they can be used to potentially distinguish between different triggering mechanisms. We also discuss the temporal anisotropy results and interpretations of Li et al., as compared to the results shown in this paper. Finally, we conclude with a short discussion on how SWS observations can be used in the monitoring of injection induced seismicity.

5. DISCUSSION

5.1 Implications for fault reactivation mechanisms

As described above, Eyre et al. (2019a) proposed a model for fault reactivation whereby aseismic slip on faults in the reservoir is the driving force in reactivating the faults, leading to the M_W 4.1 mainshock. However, they did not investigate alternative potential triggering mechanisms. The modelling work presented above suggests that the observed changes in seismic anisotropy are most consistent with the stress changes in the overburden that would be generated by tensile opening of hydraulic fractures. It is therefore of interest to compare the fault reactivation potential for the hydraulic fracturing and aseismic slip patch models.

Fault reactivation due to subsurface stress changes is typically considered within the framework of perturbations in the Coulomb Failure Stress, ΔCFS (Equation 1). A positive ΔCFS implies that conditions on a fault have moved towards the failure envelope, increasing the likelihood that slip will occur, while a negative ΔCFS implies a move away from failure conditions. Hence, perturbations that create significant positive changes in ΔCFS can be thought of as representing plausible mechanisms for generating induced seismicity.

In Figure 8 we plot the ΔCFS, as resolved onto the M_W 4.1 mainshock fault plane, produced by the LOHF and aseismic slip models. The ΔCFS maps are plotted at 2,130 mbsl, the depth of the mainshock hypocentre. Both models produce positive ΔCFS changes at the mainshock hypocentre prior to its occurrence, indicating that both mechanisms represent potential causal mechanisms for triggering the induced seismicity. A wide range of ΔCFS values have been invoked as being necessary to reactivate faults, from 0.001 to 0.5 MPa (e.g., Kilb et al., 2002; Freed, 2005; Shapiro et al., 2006). The 0.15 < MPa < 0.3 MPa ΔCFS changes produced by both models are above triggering thresholds that have previously been invoked to account for fault reactivation during hydraulic fracturing (e.g., Deng et al., 2016; Kettlety et al., 2019; Kettlety et al., 2020).

We can further investigate the plausibility of both potential mechanisms by evaluating the temporal evolution ΔCFS produced by each model. For the tensile hydraulic fracture LOHF model, we simulate the cumulative ΔCFS at the mainshock hypocentre as each stage is emplaced. To assess the temporal evolution of ΔCFS for the aseismic slip model, we assume that slip on patches 1 – 5 (see Figure 5c) occurs at a constant rate during stimulation of Stages 1 – 22, and that slip on patch 6 occurs at a constant rate during stimulation of Stages 23 – 26.

Figure 9 shows the modelled temporal evolution of ΔCFS at the mainshock hypocentre. Both models produce small ΔCFS changes during the early stages of stimulation, with ΔCFS increasing sharply in the 24 hours prior to the mainshock. Hence, the modelled temporal evolutions of ΔCFS produced both by the tensile hydraulic fracture opening and the aseismic slip patch models are both consistent with the timing of the M_W 4.1 mainshock.

Hence, with respect to the timing and magnitude of ΔCFS changes produced on the fault responsible for the M_W 4.1 mainshock, both aseismic slip on reservoir faults (as proposed by Eyre et al., 2019a) and stress changes produced by tensile hydraulic fracturing are both plausible candidates for generating the induced seismicity that was observed at this site. In the absence of further geophysical observations it would be challenging to further discriminate between the relative importance of these two phenomena. However, as shown in Figure 7, the overburden stress changes from the tensile hydraulic fracture model produce a much better match to the observed seismic anisotropy changes than do the overburden stress changes from the aseismic slip model. As such, this indicates that the stress changes from tensile hydraulic fracture opening were the dominant process affecting rocks in the overburden, and were therefore the predominant cause of the fault reactivation. However, we note that, in making this conclusion, it is entirely plausible that several factors including stress changes from tensile hydraulic fracture opening; aseismic slip on reservoir faults, and indeed pore pressure migration along faults (e.g., Igonin et al., 2021) could all have jointly contributed to the fault reactivation that produced the M_W 4.1 mainshock.

5.2. Li et al. (2019)

Li et al. (2019) performed a study of changes in seismic anisotropy using data recorded by four broadband seismometers that were also deployed at this site (Figure 1). They found that main temporal change in the anisotropy occurred after the M_W 4.1 mainshock, and they hypothesized that the SWS changes were generated by a loss of fluids from the hydraulic fracture system into the fault, which caused the hydraulic fractures to close. However, the small number of stations used by Li et al. limits the number of measurement points used in their analysis. Of the four broadband stations, WSK01 was discarded by Li et al. as being beyond the shear-wave window (Booth and Crampin, 1985). Stations WSK02 and WSK04 are more than 4 km laterally from the well, while the events are located at a depth below ground of approximately 3 km, so it is difficult to determine if these stations are within the shear-wave window. The results obtained by Li et al. (2019) did not show any temporal changes at stations WSK02 and WSK03, and the only evidence for any temporal change found by Li et al. (2019) came from six measurements made at station WSK04. However, these temporal changes were associated with different clusters of events, and their method did not account for normalising the observed delay times by path length. As such, it is unclear whether the changes they observed actually represent a change in anisotropy, or simply a change in the loci of events used to make the measurements, since a change in path length will produce a change in δt even if there is no change in the strength of the anisotropy. For this reason, we stress the importance of normalisation in our results.

With respect to the physical mechanism proposed by Li et al. (2019), the microseismic events on which SWS measurements were made are located in the overlying Ireton and Wabamun Formations, with an upward raypath to the near-surface stations. As such, no part of the raypath could have sampled the reservoir, and so any changes in anisotropy cannot have been generated directly by hydraulic fractures themselves (except through the impact of the stress changes they might generate in overlying strata, as we have demonstrated). As such, the hypothesis proposed Li et al. (2019) may not be plausible.

We proposed and tested several hypotheses in our study because we were able to make use of thousands of SWS measurements recorded on a dense surface array, which affords us the resolution to investigate in detail the spatial and temporal changes in anisotropy. While we have observed some changes in anisotropy at some stations associated with the M_W 4.1 mainshock, we show that many stations showed a gradual temporal evolution through time as the hydraulic fracturing progressed, prior to the occurrence of the mainshock. Similarly, the dense spatial coverage has allowed us to characterise the spatial distribution of anisotropy changes, where some regions experienced increases in anisotropy, and others experienced decreases, at the same time. Such changes cannot be accounted for by the Li et al. fracture closure model, however as we have demonstrated, they are entirely consistent with the stress changes we would expect to occur around and above tensile-opening hydraulic fractures.

5.3. Implications for injection induced seismicity

To date, SWS measurements on microseismic datasets during hydraulic fracturing have primarily been performed using downhole monitoring arrays placed in or near the reservoir. As such, raypaths are predominantly through reservoir rocks, allowing us to directly image sedimentary structures (e.g., Baird et al., 2017) and fracturing (e.g., Verdon et al., 2010; Wuestefeld et al., 2011; Verdon and Wuestefeld, 2013; Baird et al., 2013; Gajek et al., 2018) within the reservoir.

For microseismic datasets recorded using surface arrays, the majority of the raypath is through the overburden, meaning that we cannot directly image hydraulic fractures within the reservoir. However, this study shows that measurements of SWS made using dense surface arrays can still provide useful information with respect to geomechanical processes occurring within the reservoir. The fact that the LOHF model, which incorporates the effects of leak-off and limitations in HF length, produces a better match to the observed SWS than the HHF model, which does not, provides independent evidence as to the interaction between the hydraulic fractures and the fault. Similarly, we have shown that different geomechanical processes occurring within the reservoir produce very different patterns of stress change that extend into the overburden, and the relative importance of these different processes can therefore be distinguished through careful observations of SWS changes made using dense surface arrays.

Although the results in this paper are related specifically to hydraulic fracturing, these methods can also be used for interpreting seismicity due to wastewater injection or carbon capture and sequestration. Since both of these processes change the subsurface stress conditions, it is possible that these changes can be monitored using SWS measurements over time.

5. CONCLUSIONS

The process of hydraulic fracturing perturbs the stress field in the target reservoir and the rocks that surround it. These perturbations can reactivate pre-existing faults, leading to induced seismicity. The occurrence of induced seismicity has posed a challenge for operations in several important shale gas plays around the world. Methods to image the stress perturbations created by hydraulic fracturing are of key importance to better understand these geomechanical processes. In this study, we have performed measurements of seismic anisotropy using SWS recorded by a dense surface monitoring array deployed above a hydraulic fracturing site in the Fox Creek region of Alberta, Canada. A M_W 4.1 event was triggered at this site, which caused the shut-down of the operation.

We observed clear and coherent temporal changes in SWS during the hydraulic fracturing process. Given that the recorded raypaths travelled almost exclusively through the overburden, stress changes generated by hydraulic fracturing are the most plausible driver of the temporal anisotropy variations. We developed several candidate models to simulate stress perturbations around the reservoir, including tensile hydraulic fracturing, microseismic slip on faults, aseismic slip on faults, and coseismic slip with the M_W 4.1 mainshock. We also developed a modified hydraulic fracturing model whereby the growth of hydraulic fractures was limited by their intersection with a known, mapped fault. We compared the results of these various models with the observed anisotropy, finding that the only case with stress perturbations that matched the positions where increases and decreases in anisotropy were observed was provided by the modified hydraulic fracture model. We then assessed the stress changes produced at the hypocentre of the M_W 4.1 mainshock, finding that this model produces significant positive ΔCFS changes at the hypocentre in the 24 hours prior to the event, and therefore represents a plausible candidate mechanism for the triggering of this event.

Data and Resources

Passive seismic data used in this study were provided by Repsol Oil & Gas Canada Inc. and are proprietary. The vendor event catalog is also proprietary and cannot be released to the public. All of the figures were made using Matlab. The supplementary material for this paper contains further details about how the fast S-wave orientation and delay time were calculated. Time series of the fast S-wave direction and delay time for each station are also included in the supplementary material.

Acknowledgements

The authors are grateful to Repsol Oil & Gas Canada Inc. for providing the microseismic data, which were processed by Magnitude. This research was supported in part by funding from NSERC through the PGS-D and the SEG Reba C. Griffin Memorial Scholarship. We thank the sponsors of the Microseismic Industry Consortium for their financial support of this study. James Verdon is supported by the UK Natural Environment Research Council (Grant Number NE/R018162/1). We would also like to thank Ryan Schultz and another anonymous reviewer for their helpful suggestions to improve this paper.

References

Atkinson, G.M., Eaton, D.W. and Igonin, N., 2020. Developments in understanding seismicity triggered by hydraulic fracturing. Nat Rev Earth Environ 1, 264–277. https://doi.org/10.1038/s43017-020-0049-7.

Alberta Energy Regulator, 2015. Subsurface Order No. 2, https://aer.ca/documents/orders/subsurface-orders/SO2.pdf

Baird, A.F., J-M. Kendall, J.P. Verdon, A. Wuestefeld, T.E. Noble, Y. Li, M. Dutko, Q.J. Fisher, 2013. Monitoring increases in fracture connectivity during hydraulic stimulations from temporal variations in shear-wave splitting polarization: Geophysical Journal International 195, 1,120-1,131.

Baird, A.F., J-M. Kendall, Q.J. Fisher, J. Budge, 2017. The role of texture, cracks and fractures in highly anisotropic shales: Journal of Geophysical Research 122, 10,341-10,351.

Bao, X. and D.W. Eaton, 2016. Fault activation by hydraulic fracturing in western Canada: Science 354, 1,406-1,409.

Booth, D.C. and S. Crampin, 1985. Shear-wave polarizations on a curved wavefront at an isotropic free surface: Geophysical Journal International 83, 31-45.

Buijze, L, L. van Bijsterveldt, H. Cremer, B. Paap, H. Veldkamp, B.B.T. Wassing, J-D. van Wees, G.C.N. van Yperen, J.H. ter Heege, B. Jaarsma, 2019. Review of induced seismicity in geothermal systems worldwide and implications for geothermal systems in the Netherlands: Netherlands Journal of Geosciences 98, e13.

Clarke, H., J.P. Verdon, T. Kettlety, A.F. Baird, J-M. Kendall, 2019. Real time imaging, forecasting and management of human-induced seismicity at Preston New Road, Lancashire, England: Seismological Research Letters 90, 1,902-1,915.

Crampin, S., 1987. Geological and industrial implications of extensive-dilatancy anisotropy: Nature, 328, 491-496.

Deng, K., Y. Liu, R.M. Harrington, 2016. Poroelastic stress triggering of the December 2013 Crooked Lake, Alberta, induced seismicity sequence: Geophysical Research Letters 43, 8,482-8,491.

Eaton, D.W., 2018. Passive seismic monitoring of induced seismicity: Cambridge University Press.

Ellsworth, W.L., 2013. Injection-induced earthquakes: Science 341, 1225942-1:7.

Eyre, T.S., D.W. Eaton, D.I. Garagash, M. Zecevic, M. Venieri, R. Weir, D.C. Lawton, 2019a. The role of aseismic slip in hydraulic fracturing-induced seismicity: Science Advances 5, eaav7172.

Eyre, T.S., D.W. Eaton, M. Zecevic, D. D'Amico, D. Kolos, 2019b. Microseismicity reveals fault activation before M_W 4.1 hydraulic-fracturing induced earthquake: Geophysical Journal International 218, 534-546.

Eyre, T.S., M. Zecevic, R.O. Salvage, D.W. Eaton, 2020. A long-lived swarm of hydraulic fracturing-induced seismicity provides evidence for aseismic slip: Bulletin of the Seismological Society of America 110, 2,205-2,215.

Freed, A.M., 2005. Earthquake triggering by static, dynamic, and postseismic stress transfer: Annual Review of Earth and Planetary Sciences 33, 335-367.

Gajek, W., M. Malinowki, J.P. Verdon, 2018. Results of downhole microseismic monitoring at a pilot hydraulic fracturing site in Poland - Part 2: S-wave splitting analysis: Interpretation 6, SH49-SH58.

Igonin, N., J.P. Verdon, J-M. Kendall, D.W. Eaton, 2021. Large-scale fracture systems are permeable pathways for fault activation during hydraulic fracturing: Journal of Geophysical Research 126, e2020JB020311.

Kanamori, H. and E.E. Brodsky, 2004. The physics of earthquakes: Reports on Progress in Physics 67, 1429-1496.

Kao, H., R. Visser, B. Smith, S. Venables, 2018. Performance assessment of the induced seismicity traffic light protocol for northeastern British Columbia and western Alberta: The Leading Edge 37, 117-126.

Kettlety, T., J.P. Verdon, M.J. Werner, J-M. Kendall, J. Budge, 2019. Investigating the role of elastostatic stress transfer during hydraulic fracturing-induced fault activation: Geophysical Journal International 217, 1200-1216.

Kettlety, T., J.P. Verdon, M. Werner, J-M. Kendall, 2020. Stress transfer from opening hydraulic fractures controls the distribution of induced seismicity: Journal of Geophysical Research 125, e2019JB018794.

Kilb, D., J. Gomberg, J., P. Bodin, 2002. Aftershock triggering by complete Coulomb stress changes: Journal of Geophysical Research 107, 2,060.

Li, T., Y. Gu, Z. Wang, R. Wang, R. Chen, T. Song, R. Wang, 2019. Spatiotemporal variations in crustal seismic anisotropy surrounding induced earthquakes near Fox Creek, Alberta: Geophysical Research Letters 46, 5180-5189.

Maxwell S., and M. Norton, 2012. Enhancing shale gas reservoir characterization using hydraulic fracture microseismic data: First Break 30, 95-101.

Okada, Y., 1992. Internal deformation due to shear and tensile faults in a half-space: Bulletin of the Seismological Society of America 82, 1,018-1,040.

Peña-Castro, A.F., M.P. Roth, A. Verdecchia, J. Onwuemeka, Y. Liu, R.M. Harrington, Y. Zhang, H. Kao, 2020. Stress chatter via fluid flow and fault slip in a hydraulic fracturing induced earthquake sequence in the Montney formation, British Columbia: Geophysical Research Letters 47, e2020GL087254.

Riazi, N. and D.W. Eaton, 2020. Anatomy of a buried thrust belt activated during hydraulic fracturing: Tectonophysics 795, 228640.

Ruiz-Barajas, S., N. Sharma, V. Convertito, A. Zollo, B. Benito, 2017. Temporal evolution of a seismic sequence induced by a gas injection in the Eastern coast of Spain: Nature Scientific Reports 7, 2,901.

Schultz, R., R. Wang, Y.J. Gu, K. Haug, G. Atkinson, 2017. A seismological overview of the induced earthquakes in the Duvernay play near Fox Creek, Alberta: Journal of Geophysical Research 122, 492-505.

Schultz, R., Skoumal, R. J., Brudzinski, M. R., Eaton, D., Baptie, B., Ellsworth, W., 2020. Hydraulic fracturing-induced seismicity. Reviews of Geophysics, 58(3), e2019RG000695, doi: 10.1029/2019RG000695.

Shapiro, S.A., C. Dinske, E. Rothert, 2006. Hydraulic-fracturing controlled dynamics of microseismic clouds. Geophysical Research Letters, 33 1-5.

Steacy, S., D. Marsan, S.S. Nalbant, J. McCloskey, 2004. Sensitivity of static stress calculations to the earthquake slip distribution: Journal of Geophysical Research 109, B04303.

Stein, R.S., 1999. The role of stress transfer in earthquake occurrence. Nature 402, 605-609.

Stork, A.L., J.P. Verdon, J-M. Kendall, 2015. The microseismic response at the In Salah Carbon Capture and Storage (CCS) site: International Journal of Greenhouse Gas Control 32, 159-171.

Teanby, N.A., J-M. Kendall, M. van der Baan, 2004. Automation of shear-wave splitting measurements using cluster analysis: Bulletin of the Seismological Society of America 94, 453-463.

Verdon, J.P. and A. Wuestefeld, 2013. Measurement of the normal/tangential compliance ratio (Z_N/Z_T) during hydraulic fracture stimulation using shear wave splitting data: Geophysical Prospecting 61, 461-475.

Verdon, J.P. and J.J. Bommer, 2021. Green, yellow, red, or out of the blue? An assessment of Traffic Light Schemes to mitigate the impact of hydraulic fracturing-induced seismicity: Journal of Seismology 25, 301-326.

Verdon, J.P., D.A. Angus, J-M. Kendall, S.A. Hall, 2008. The effects of microstructure and nonlinear stress on anisotropic seismic velocities: Geophysics 73, D41-D51.

Verdon, J.P., J-M. Kendall, A. Wuestefeld, 2009. Imaging fractures and sedimentary fabrics using shear wave splitting measurements made on passive seismic data: Geophysical Journal International 179, 1,245-1,254.

Verdon, J.P., J-M. Kendall, S.C. Maxwell, 2010. A comparison of passive seismic monitoring of fracture stimulation due to water versus CO_2 injection: Geophysics 75, MA1-MA7.

Wang, R., F. Lorenzo Martin, F. Roth, 2006. PSGRN/PSCMP - a new code for calculating co- and post-seismic deformation, geoid and gravity changes based on the viscoelastic-gravitational dislocation theory: Computers and Geosciences 32, 527-541.

Wang, R., Y.J. Gu, R. Schultz, A. Kim, G. Atkinson, 2016. Source analysis of a potential hydraulic fracturing induced earthquake near Fox Creek, Alberta: Geophysical Research Letters 43, 564-573.

Wang, R., Gu, J., Schultz, R., Zhang, M., Kim, A., 2017. Source characteristics and geological implications of the January 2016 induced earthquake swarm near Crooked Lake, Alberta: Geophysical Journal International 210(2), 979-988.

Wuestefeld, A., J.P. Verdon, J-M. Kendall, J. Rutledge, H. Clarke, J. Wookey, 2011. Inferring rock fracture evolution during reservoir stimulation from seismic anisotropy: Geophysics 76, WC159-WC168.

Zatsepin, S., and S. Crampin, 1997. Modelling the compliance of crustal rock - I. Response of shear-wave splitting to differential stress: Geophysical Journal International 129, 477-494.

POSTAL ADDRESSES

Nadine Igonin, Jackson School of Geosciences, 2305 Speedway Stop C1160, Austin, TX 78712-1692.

James Verdon, School of Earth Sciences, University of Bristol, Wills Memorial Building, Queen's Road, Bristol, UK, BS8 1TH.

David Eaton, Department of Geoscience, 2500 University Drive NW, Calgary, Alberta, Canada, T2N 1N4.

TABLES

Table 1: Summary of the six model scenarios used to simulate stress and anisotropy changes around the Waskahigan wells.

	Model Name	**Model Overview**
1	Tensile HF	This model simulates stress changes generated by tensile opening of hydraulic fractures around the well.
2	Tensile HF with leak-off	As above, but the geometry of tensile hydraulic fractures is adjusted to reflect (i) the predominantly eastward HF propagation, and potential limits on HF propagation at the toe of the well due to potential intersection with observed faults.
3	Aseismic fault slip – strike slip	This model simulates aseismic right-lateral slip along the observed NE-trending fault structures, as postulated by Eyre et al. (2019a).
4	Observed Microseismicity	This model computes stress changes that would be generated by the observed microseismic events, with slip amounts determined by event magnitudes, and slip orientations determined by observed source mechanisms.
5	Aseismic fault slip – dilatant	This model simulates aseismic dilation along the observed NE-trending fault structures: this dilation might be expected as elevated pore pressures in the reservoir intersect the faults.
6	Coseismic with mainshock	This model simulates the co-seismic stress changes that would be generated by the M_W 4.1 mainshock. The slip amount is based on the event magnitude, and the slip orientation is based on the observed focal mechanism.

FIGURES

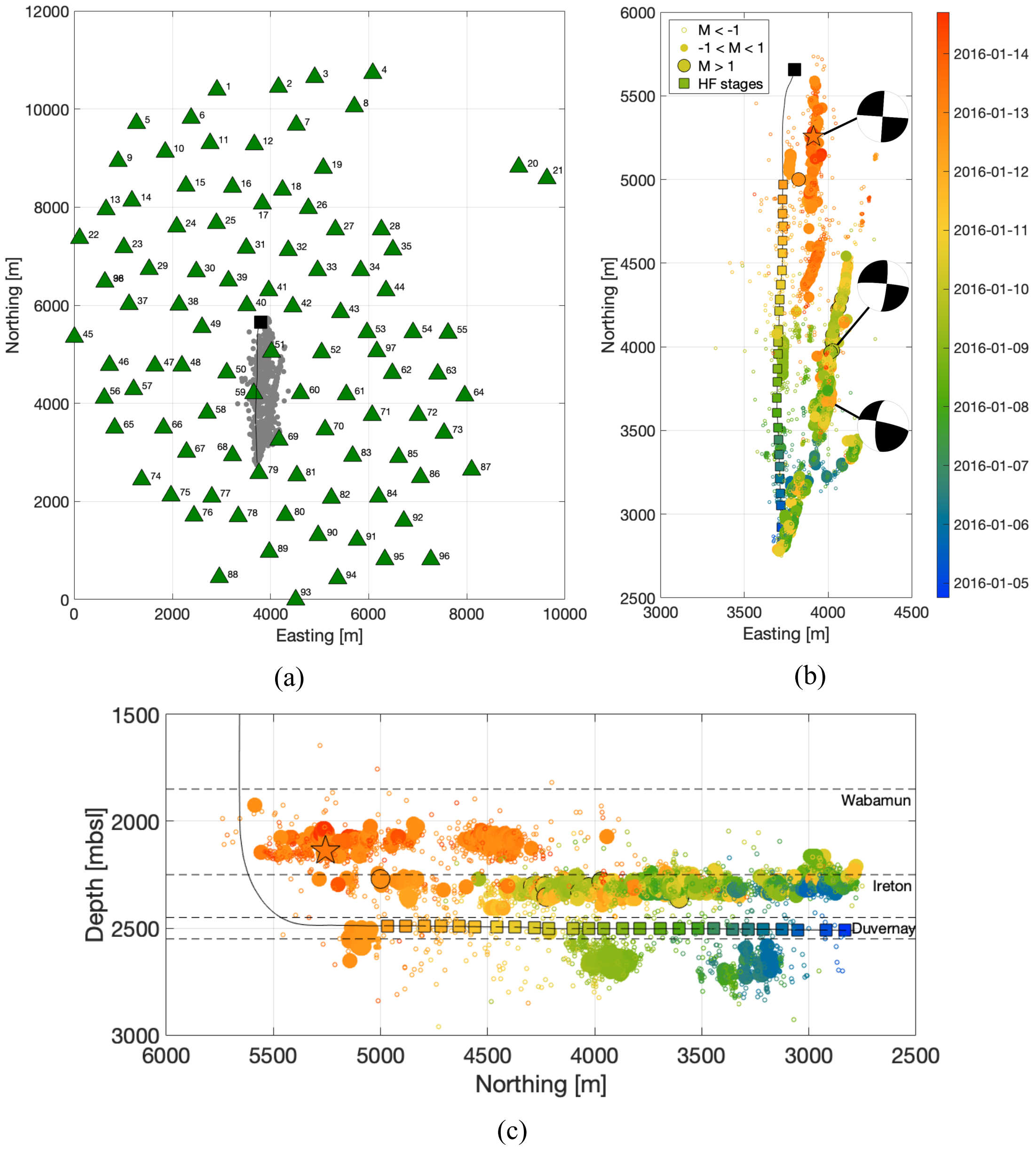

Figure 1: The Waskahigan microseismic dataset: in (a) we show a map of the well (black square and line), monitoring stations (green triangles) and events grey dots. In (b) we show a map of the recorded events, showing event locations (circles coloured by occurrence time and sized by magnitude), and locations of each injection stage (squares coloured by the start time of each stage) along the well (black line). The hypocenter of the M_W 4.1 event is shown by the star. The focal mechanisms for the three largest events are also shown (Wang et al., 2017). In (c) we show a cross section of event and injection stage locations. The approximate depths of the Duvernay, Ireton and Wabamun Formations are marked by the black dashed lines.

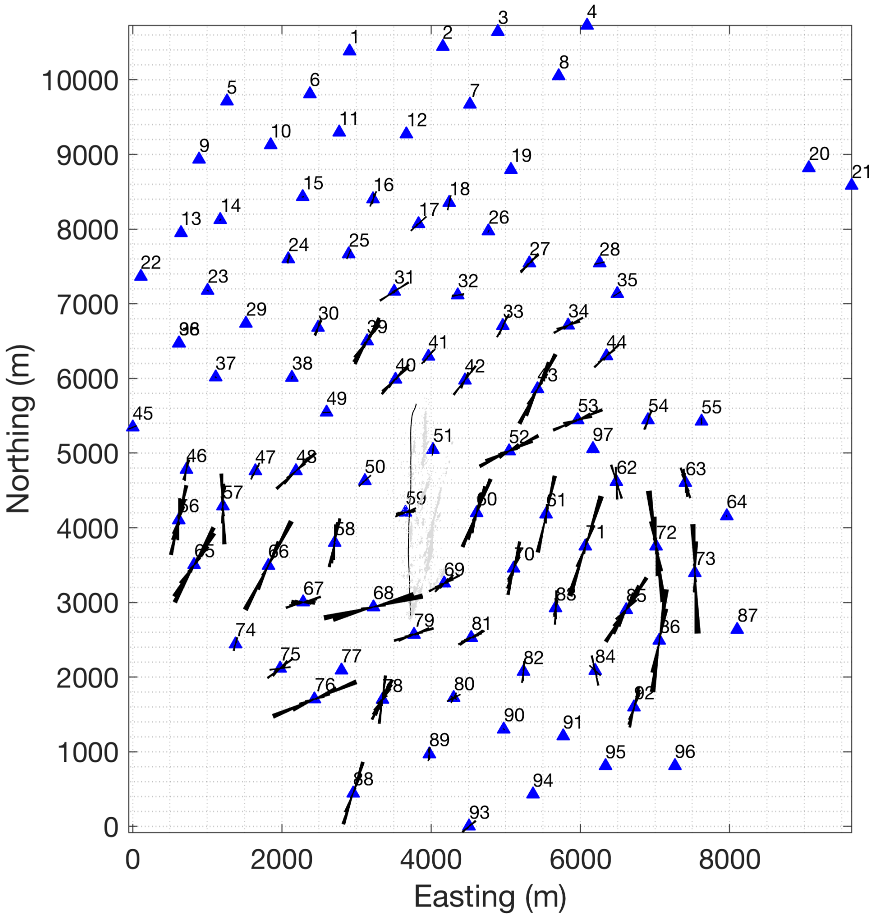

Figure 2: Map of fast S-wave polarization direction at each station. Rose diagrams show values of anisotropy orientation, binned at 5-degree increments. Size of rose diagram denotes number of measurements at each station, with many of the distal stations having no results that passed the quality control criteria.

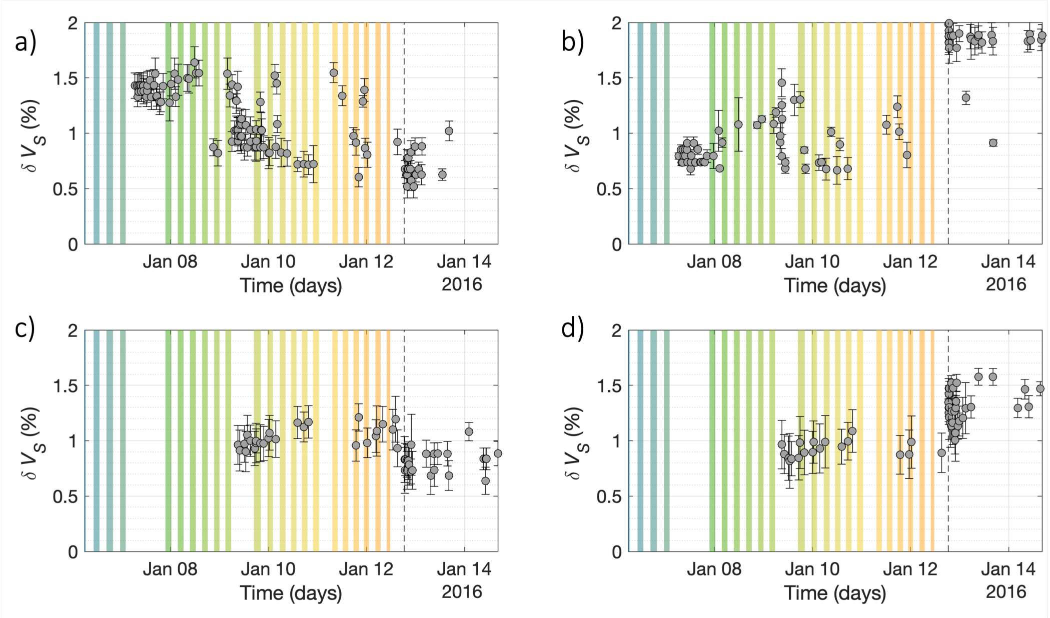

Figure 3: Examples showing stations that experienced temporal changes in δV_S during the stimulation: Station 71 (a), 58 (b), 44 (c), 34 (d). Stations 71 and 58 experienced increases and decreases in δV_S prior to the M_W 4.1 mainshock on Jan 12, while Stations 34 and 44 experienced increases and decreases in δV_S that were co-seismic with the mainshock. The background shaded regions correspond to the times of stages 6 to 26 and match the color scale in Figure 1. Vertical lines from the measurement points indicate the uncertainty.

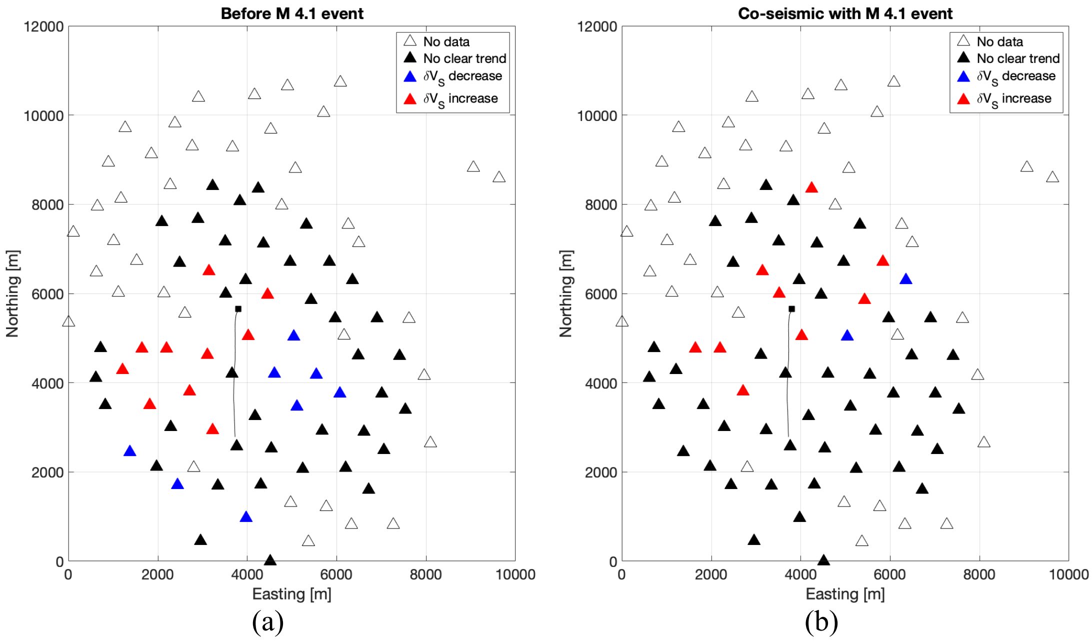

Figure 4: Observed changes in anisotropy strength (δV_S) during stimulation prior to the M_W 4.1 mainshock, and co-seismic with the mainshock; stations which show a clear increase are plotted in red, those that show a decrease are plotted in blue, stations for which no clear trend was observed are shown in black, and stations for which no SWS measurements were returned are shown in white.

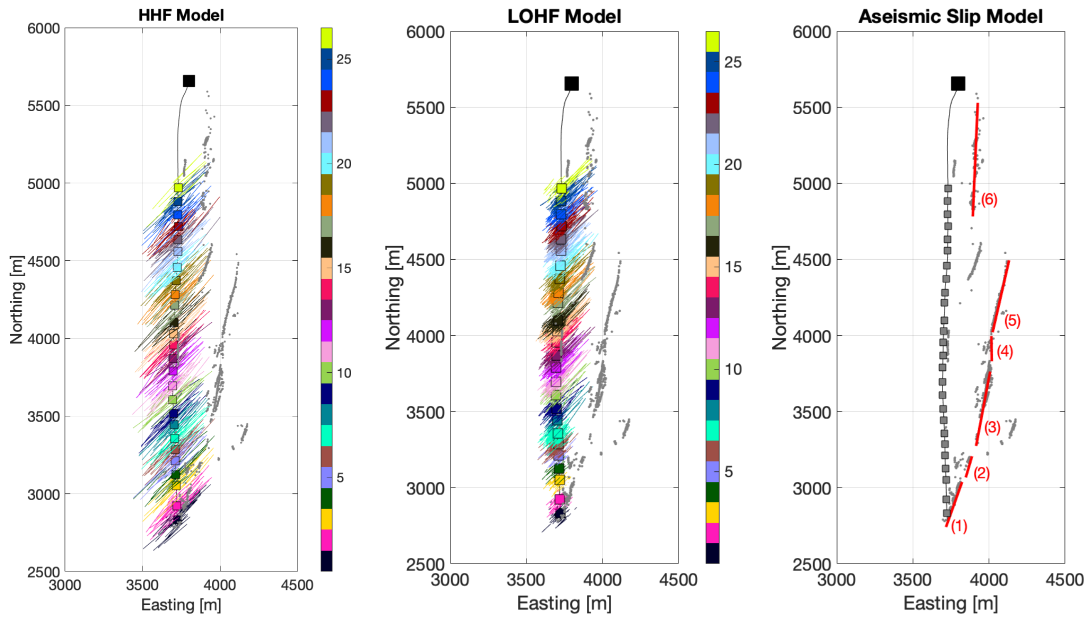

(a) (b) (c)

Figure 5: In (a) we show an example of a stochastically-generated HHF hydraulic fracture model used to simulate the impacts of tensile fracture opening. In map view, we show the injection points (squares) coloured by stage number, with the modelled fractures shown as coloured lines extending from each injection point. In (b) we show an example of the alternative LOHF model, which accounts for the potential impacts of the intersection between hydraulic fractures and the structures at the toe of the well. In (c) we show the positions of the aseismic slip patches (red lines numbered 1 – 6) used to simulate the stress perturbations created by aseismic slip. Patches 1 – 5 represent the large NNE-trending structure, and patch 6 represents the N-S striking fault at the heel of the well. In all plots, observed microseismic events with M > -1 are also shown as grey dots.

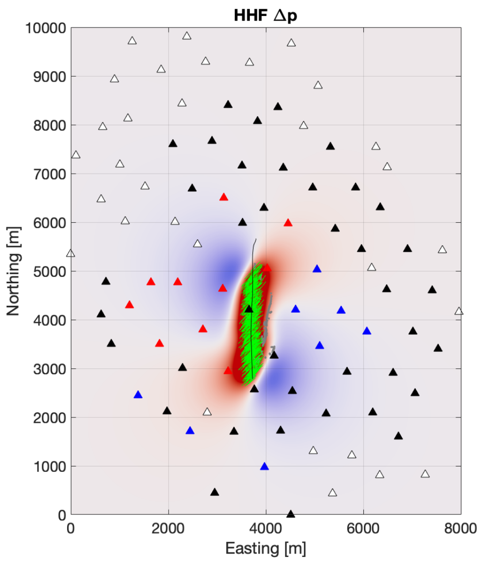
HHF Δp
Northing [m]
Easting [m]

(a)

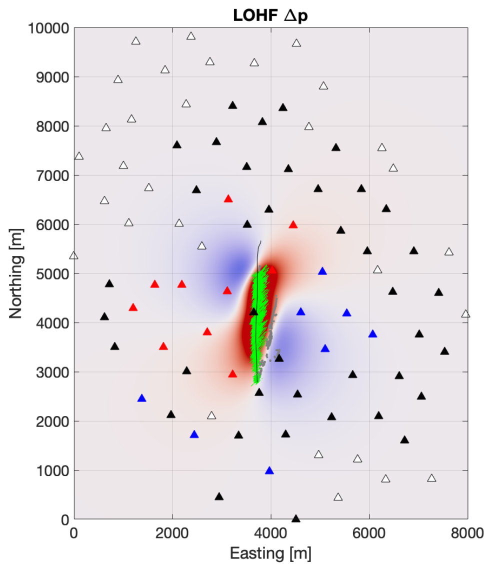
LOHF Δp
Northing [m]
Easting [m]

(b)

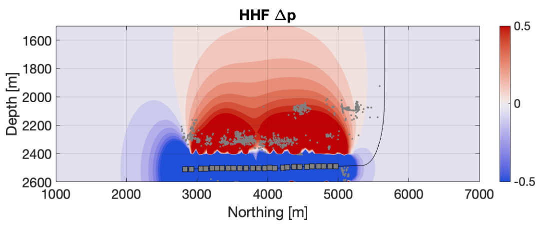
HHF Δp
Depth [m]
Northing [m]

(c)

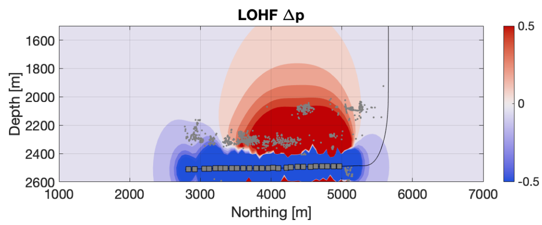
LOHF Δp
Depth [m]
Northing [m]

(d)

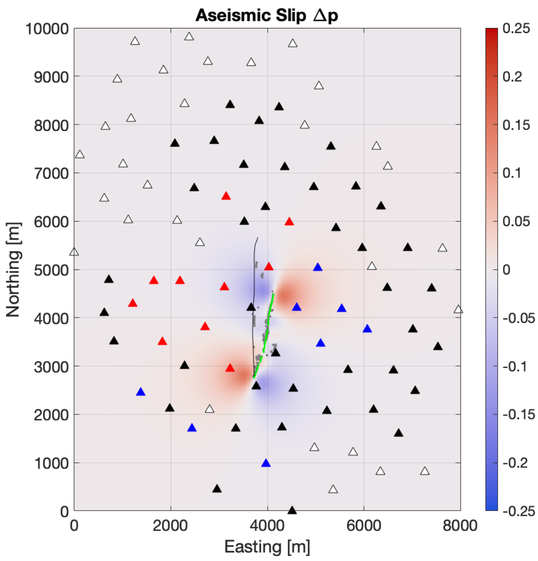
Aseismic Slip Δp
Northing [m]
Easting [m]

(e)

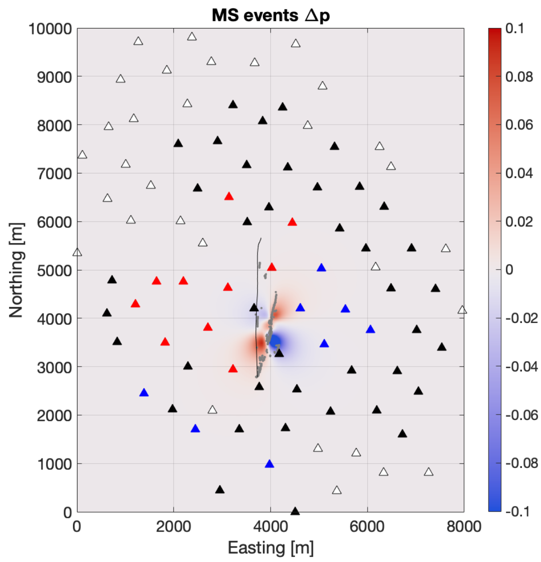
MS events Δp
Northing [m]
Easting [m]

(f)

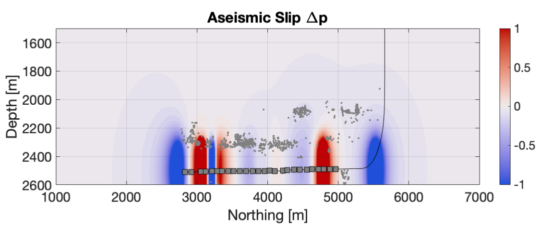
Aseismic Slip Δp
Depth [m]
Northing [m]

(g)

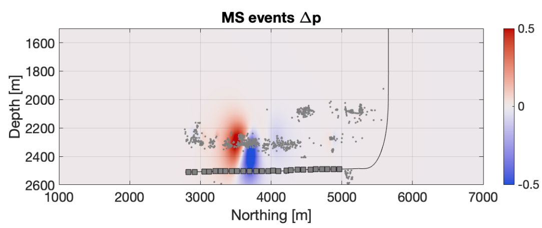
MS events Δp
Depth [m]
Northing [m]

(h)

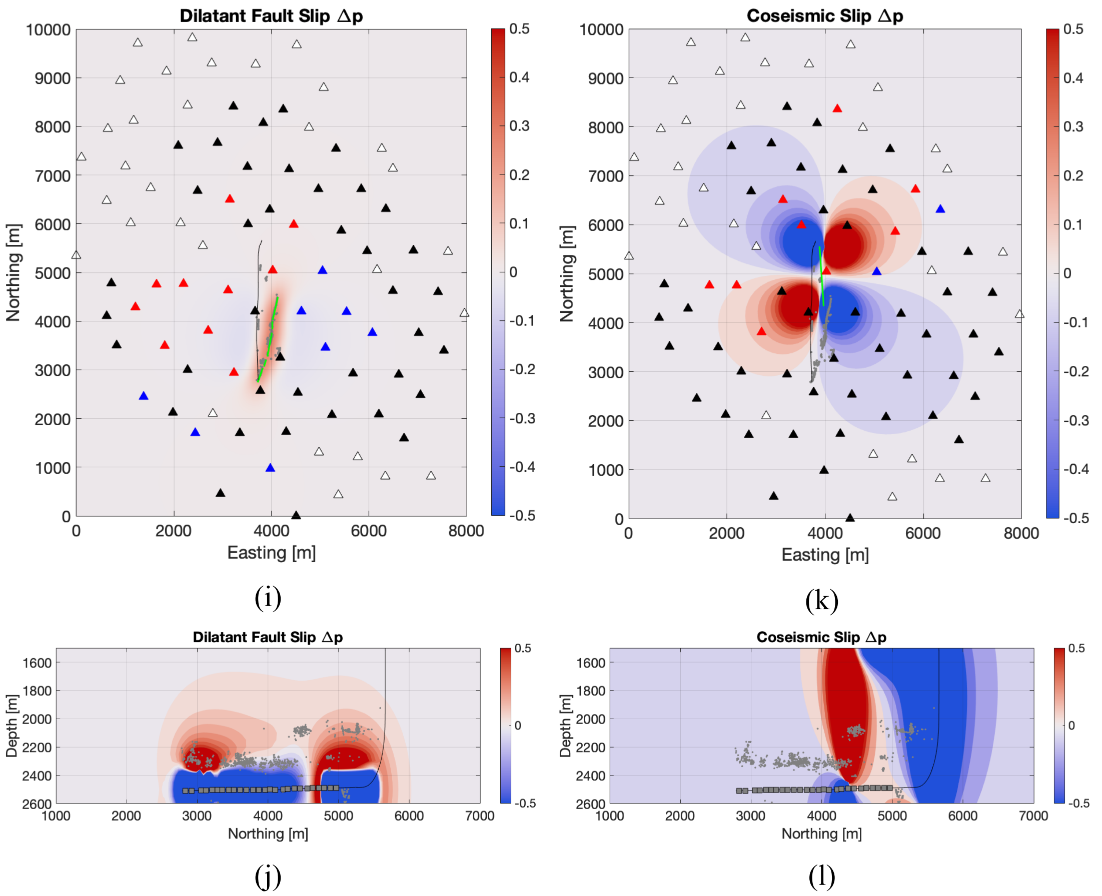

Figure 6: Maps (a, b, e, f, i, k) and cross sections (c, d, g, h, j, l) showing the changes in mean principal stress, Δp (in MPa), generated by the HHF (a,c), LOHF (b,d), aseismic slip (e, g), microseismic slip (f, h), dilatant fault slip (i, j) and coseismic slip with the M_W 4.1 mainshock (k, l) models. The maps show the stress changes at a depth of 2,100 mbsl, and the cross-sections are plotted along a line of y = 3,825 m. In the map plots, the locations of monitoring stations are shown, coloured by the observed temporal changes in SWS prior to the M_W 4.1 mainshock (a, b, e, f, i) and the M_W 4.1 coseismic changes (k), as per Figure 4. Microseismic event locations are shown with grey dots, and the well with a black solid line.

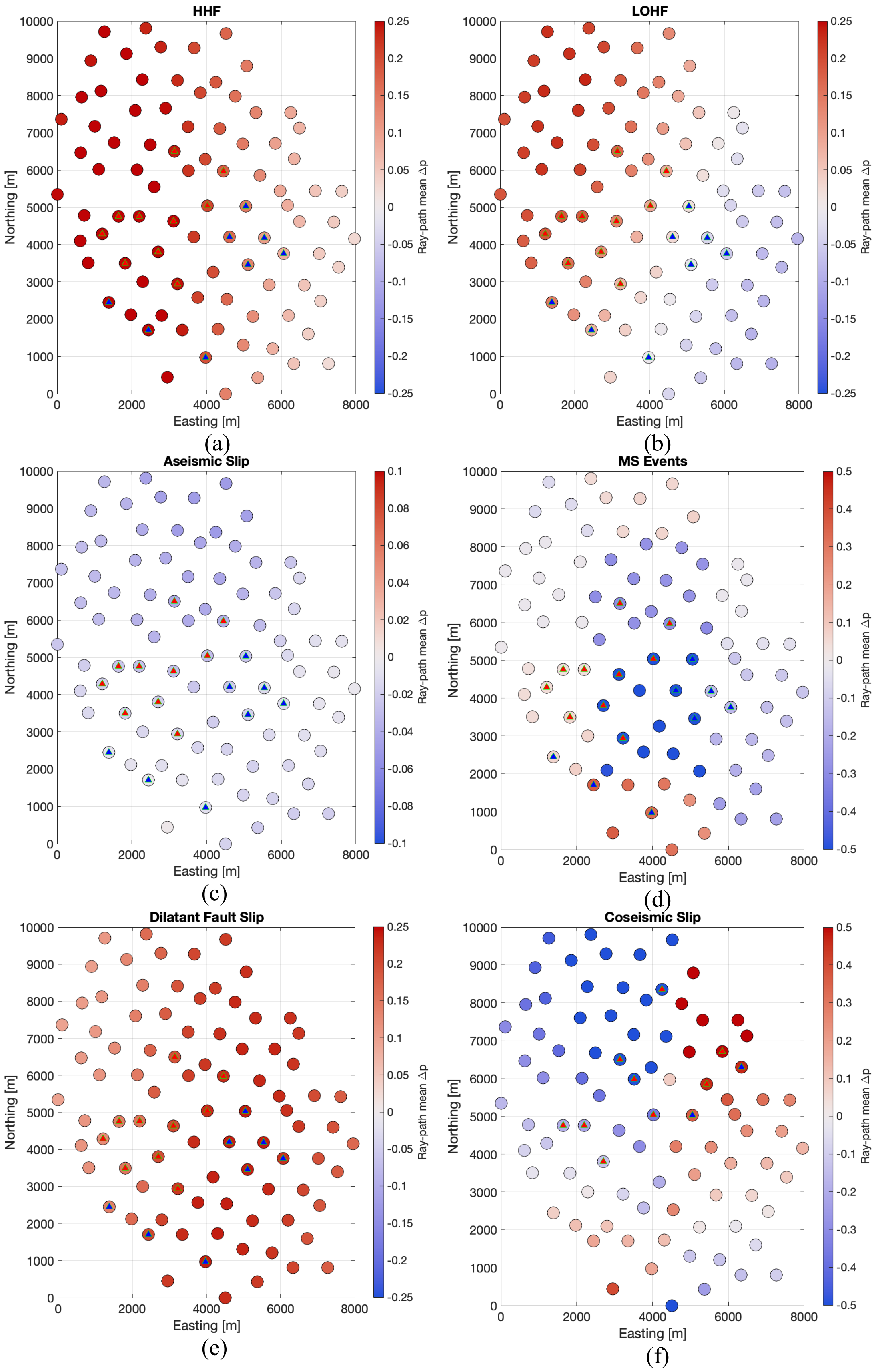

Figure 7: Average Δp along the raypaths to each station (coloured circles) for each stress model: HHF (a); LOHF (b); aseismic slip (c); microseismic events (d); dilatant fault slip (e);

and coseismic slip (f). We also plot the observed changes in δV_S for stations where a measurable trend was observed (green-outlined triangles) as per Figure 4.

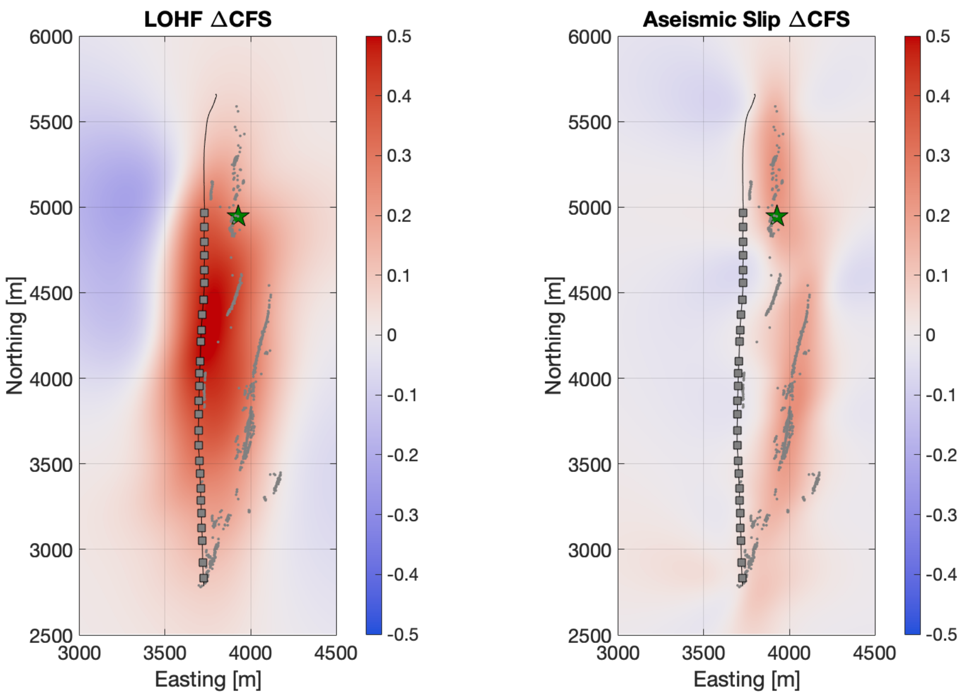

(a) (b)

Figure 8: Modelled ΔCFS changes produced by (a) tensile opening of hydraulic fractures (LOHF model), and (b) aseismic slip patches, plotted at the depth of the M_W 4.1 mainshock. The mainshock location is marked by the green star. The well and injection points are marked (black line and grey squares), as are the positions of all $M_W > -1$ events (grey dots).

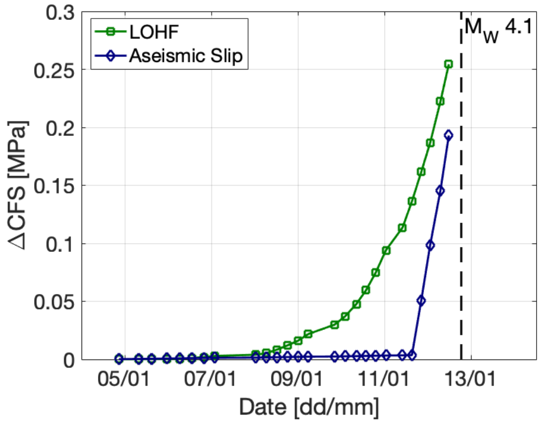

Figure 9: Modelled temporal evolution of ΔCFS at the M_W 4.1 mainshock hypocenter, prior to the occurrence of this event, as generated by the tensile hydraulic fracture LOHF model (green squares) and the aseismic slip model (blue diamonds). The symbols along each curve are placed at the start-time of each fracturing stage (from 1 to 26). The timing of the mainshock is shown by the vertical dashed line.